



This is a repository copy of *Geometrical statistics of fluid deformation: Restricted Euler approximation and the effects of pressure*.

White Rose Research Online URL for this paper:  
<http://eprints.whiterose.ac.uk/97393/>

Version: Accepted Version

---

**Article:**

Li, Y. (2012) Geometrical statistics of fluid deformation: Restricted Euler approximation and the effects of pressure. *Comptes Rendus Physique*, 13 (9-10). pp. 878-888. ISSN 1631-0705

<https://doi.org/10.1016/j.crhy.2012.09.003>

---

© 2012 Académie des sciences. Published by Elsevier Masson SAS. This is an author produced version of a paper subsequently published in *Comptes Rendus Physique*. Uploaded in accordance with the publisher's self-archiving policy. Article available under the terms of the CC-BY-NC-ND licence (<https://creativecommons.org/licenses/by-nc-nd/4.0/>)

**Reuse**

This article is distributed under the terms of the Creative Commons Attribution-NonCommercial-NoDerivs (CC BY-NC-ND) licence. This licence only allows you to download this work and share it with others as long as you credit the authors, but you can't change the article in any way or use it commercially. More information and the full terms of the licence here: <https://creativecommons.org/licenses/>

**Takedown**

If you consider content in White Rose Research Online to be in breach of UK law, please notify us by emailing [eprints@whiterose.ac.uk](mailto:eprints@whiterose.ac.uk) including the URL of the record and the reason for the withdrawal request.



[eprints@whiterose.ac.uk](mailto:eprints@whiterose.ac.uk)  
<https://eprints.whiterose.ac.uk/>

# Geometrical statistics of fluid deformation: restricted Euler approximation and the effects of pressure

Yi Li

*School of mathematics and statistics, University of Sheffield, Sheffield, UK, S3 7RH*

---

## Abstract

The geometrical statistics of fluid deformation are analyzed theoretically within the framework of the restricted Euler approximation, and numerically using direct numerical simulations. The restricted Euler analysis predicts that asymptotically a material line element becomes an eigenvector of the velocity gradient regardless its initial orientation. The asymptotic stretching rate equals the intermediate eigenvalue of the strain rate tensor. Analyses of numerical data show that the pressure Hessian is the leading cause to destroy the alignment between the longest axis of the material element and the strongest stretching eigen-direction of the strain rate. It also facilitates the alignment between the longest axis of the element and the intermediate eigen-direction of the strain rate during initial evolution, but tends to oppose the alignment later.

---

## 1. Introduction

Enhanced mixing is a prominent feature of turbulent flows. At the smallest scales, mixing is related to the stretching and evolution of infinitesimal material elements, such as lines, surfaces and volumes. Thus the latter has been the focus of a number of previous works [1, 2, 3, 4, 5, 6, 7, 8, 9, 10, 11]. The evolution of material elements carries useful information for model construction, as is demonstrated in [12, 13, 14, 15] for velocity gradients, and [16] for subgrid-scale models. These developments further contribute to the interests in the study of the Lagrangian evolution of material elements.

One of the central problems in the above investigations is the stretching rate of the material elements. It is closely related to the geometry of the elements as well as the small scales of turbulence. Small scales of the turbulent field are described by the velocity gradient tensor  $A_{ij} \equiv \partial u_i / \partial x_j$ , where  $u_i(\mathbf{x}, t)$  is the velocity field, the strain rate tensor  $S_{ij} \equiv (A_{ij} + A_{ji})/2$ , and the vorticity  $\omega_i = \epsilon_{ijk} A_{kj}$ . The equation for  $A_{ij}$  can be derived from the Navier-Stokes (NS) equation and is given as:

$$\frac{dA_{ij}}{dt} = -A_{ik}A_{kj} - \partial_{ij}^2 p + \nu \nabla^2 A_{ij} \quad (1)$$

where  $p$  is the pressure,  $\partial_{ij}^2 p \equiv \partial^2 p / \partial x_i \partial x_j$  is the pressure Hessian. The density of the fluid is assumed to be 1 and  $\nu$  is the viscosity. One important geometrical statistic is the alignment between a material line element and the eigenvectors of the strain rate tensor. Let  $l_i$  denote the  $i$  component of a material line element, then

$$\frac{dl_i}{dt} = A_{ij} l_j. \quad (2)$$

The growth in the length of  $l_i$  is measured by the logarithmic rate of change  $d \ln l / dt$  where  $l \equiv (l_i l_i)^{1/2}$  is the length of  $l_i$ . It follows from the above equation that

$$\frac{d \ln l}{dt} = \hat{l}_i A_{ij} \hat{l}_j = \hat{l}_i S_{ij} \hat{l}_j \quad (3)$$

where  $\hat{l}_i \equiv l_i / l$  is the direction of the element. Thus the growth rate is closely related to the alignment between  $l_i$  and  $S_{ij}$ .

The alignment problem has been addressed in [4, 5, 6, 9, 10], among others. [4] analyze the non-persistent nature of the alignment and its effects on the mean stretching rate. The dynamics of the alignment is considered in [5] based on the equation for the direction cosines of a line element made with the eigenvectors of the strain rate tensor. Results in simple flow fields and random Gaussian velocity fields are discussed. The strong alignment with the intermediate stretching eigendirection of the strain rate tensor is observed in [6, 8]. It is also found that the alignment with the strongest stretching direction is also preferred albeit to a somewhat lesser extent. To understand the alignment statistics of material line elements as well as vorticity, [10] looks into the rotation of the eigenvectors and the switching events during the Lagrangian evolution of material elements. They find that the active role of vorticity and the effect of viscous diffusion make important differences. To understand the effects of viscous diffusion, alignment of passive diffusive vectors are simulated in [9] and [17], qualitatively same alignment trends are observed. Interestingly, in Gaussian velocity fields, the strongest alignment occurs along the strongest stretching direction [17]. The result suggests that the alignment in real turbulence results from the nonlinear interaction in turbulent fields, and viscosity may not play the dominant role.

We present in this paper a further analysis of the evolution of the material line elements. We first look into the evolution of a material line in the restricted Euler (RE) approximation [18, 19, 20]. The restricted Euler equation for the velocity gradient  $A_{ij}$  makes the assumption that the pressure Hessian is isotropic. Since the pressure Laplacian is locally determined by  $A_{ij}$ , the restricted Euler equation is closed. The closed form solutions of the equations have been found and shown to become singular at finite time. Nevertheless, the solution shows that asymptotically the strain rate tensor will have a positive intermediate eigenvalue. Meanwhile the vorticity will tend to align with the intermediate eigenvector. Both are consistent with observations in turbulence, in particular in regions with strong straining. It is shown in [21] that a close form solution for the material deformation also exists in the restricted Euler approximation. However, the asymptotic behavior of the solution is not yet explored. We will look into this problem and show that, regardless of the initial orientation of the

line element, asymptotically it will become an eigenvector of the velocity gradient. The result sheds further light on the effects of the nonlinear interactions on the alignment statistics as well as the stretching rate of material lines.

We then present a DNS analysis of the dynamics of the alignment between material elements and the strain rate tensor. In particular we discuss the effects of the pressure Hessian, which has not been studied before. The pressure Hessian has been shown to play a central role in the dynamics of the velocity gradients (see, e.g., [15, 22, 23, 24, 25]). Our results show that its effects on material deformation are also significant and depend non-trivially on the relative orientation between the element and the strain rate tensor.

## 2. Material deformation in restricted Euler equations

### 2.1. Exact solution for a material line element

Infinitesimal material line elements evolve according to Eq. 2. Alternatively, evolution of material elements can be described by the deformation gradient  $B_{ij}(\mathbf{X}, t) \equiv \partial x_i(\mathbf{X}, t)/\partial X_j$ , where  $\mathbf{X}$  is the spatial coordinates of a fluid particle at some initial time  $t_0$ .  $B_{ij}$  is governed by the equation

$$\frac{dB_{ij}}{dt} = A_{ik}B_{kj}. \quad (4)$$

The evolution of line elements is determined by  $B_{ij}$  through the relation  $l_i(\mathbf{X}, t) = B_{ij}(\mathbf{X}, t)l_j(\mathbf{X}, t_0)$ . We will also use the Cauchy-Green (CG) tensor, denoted as  $\mathbf{C}$  and defined by  $C_{ij} = B_{ik}B_{jk}$ . It is easy to show that  $|l_i(t_0)|^2 = l_i C_{ij}^{-1} l_j$ , which for constant  $|l_i(t_0)|$  represents an ellipsoid. Therefore an infinitesimally small sphere evolves into an ellipsoid described by the CG tensor. The square roots of the eigenvalues of the CG tensor give the lengths of the axes of the ellipsoid, and the eigenvectors define the directions of the axes.

The restricted Euler approximation considers the inviscid case and makes the assumption that the anisotropic part of the pressure Hessian is negligible, so that

$$\partial_{ij}^2 p \approx \frac{1}{3} \nabla^2 p \delta_{ij} = -\frac{2}{3} Q \delta_{ij} \quad (5)$$

where  $Q = -A_{ij}A_{ji}/2$  is the second tensor invariant of  $A_{ij}$ . Thus the restricted Euler equation for  $A_{ij}$  becomes

$$\frac{dA_{ij}}{dt} = -A_{ik}A_{kj} - \frac{2}{3} Q \delta_{ij} \quad (6)$$

which is a closed tensorial Riccati equation for  $A_{ij}$ .

The solutions of Eq. 6 have been extensively discussed in [18, 19, 20]. The properties have been summarized in the introduction. Material deformation with restricted Euler approximation is investigated in [21]. It is shown that the deformation gradient has a closed form solution as well when the velocity gradient  $A_{ij}$  is a solution to the restricted Euler equation. The short time evolution is compared with DNS data.

We now summarize the main ideas of the solution and look into its asymptotic properties. While it is the evolution of  $B_{ij}$  that is considered in [21], the same argument applies to the line element  $l_i$ . We will illustrate the method using the latter. Let  $R = -A_{ij}A_{jk}A_{ki}/3$  be the other invariant of  $A_{ij}$ , the equations for  $R$  as well as  $Q$  in RE approximation can be found as

$$\frac{dQ}{dt} = -3R, \quad \frac{dR}{dt} = \frac{2}{3}Q^2, \quad (7)$$

which is called the trace dynamics [26]. It is not difficult to show that  $\Delta \equiv 27R^2/4 + Q^3$  is an invariant of the system. Let  $Q_0$  be the value of  $Q$  when  $R = 0$ , one has

$$\frac{27}{4}R^2 + Q^3 = Q_0^3. \quad (8)$$

Making use of the trace dynamics, and taking the derivative of Eq. 6 with respect to  $t$ , one find

$$\frac{d^2 A_{ij}}{dt^2} + \frac{2}{3}Q A_{ij} = 0. \quad (9)$$

The equation can be transformed to a linear one by changing the independent variable to  $R$ , making use of the trace dynamics (Eq. 7). The solution can thus be found in terms of hypergeometric functions.

The solution will be given in non-dimensional variables. Using  $Q_0$ , one defines a time scale  $t^* \equiv 1/|Q_0|^{1/2}$ . All the variables (except for  $l_i$ , which we keep as dimensional) are then non-dimensionalized by a suitable power of  $t^*$ . (Another  $Q$  value can be chosen in place of  $Q_0$  if the latter is zero.) We will use lower-case letters to denote the dimensionless variables, and  $\tau = t/t^*$  the dimensionless time. Then the solution for dimensionless velocity gradient  $a_{ij}$  is

$$a_{ij}(\tau) = C_{ij}f_1[r(\tau)] + D_{ij}f_2[r(\tau)], \quad (10)$$

where  $C_{ij}$  and  $D_{ij}$  are two constant coefficient matrices,  $r$  is the dimensionless invariant  $R$ , and  $f_1$  and  $f_2$  are two hypergeometric functions, whose expressions are given as, when  $Q_0 > 0$ ,

$$f_1^+(r) = \frac{1}{2} \left[ \left( 1 + \frac{3\sqrt{3}}{2}r \right)^{\frac{1}{3}} + \left( 1 - \frac{3\sqrt{3}}{2}r \right)^{\frac{1}{3}} \right], \quad (11)$$

$$f_2^+(r) = \frac{1}{\sqrt{3}} \left[ \left( 1 + \frac{3\sqrt{3}}{2}r \right)^{\frac{1}{3}} - \left( 1 - \frac{3\sqrt{3}}{2}r \right)^{\frac{1}{3}} \right], \quad (12)$$

when  $Q_0 < 0$ ,

$$f_1^-(r) = \left( 1 + \frac{27}{4}r^2 \right)^{\frac{1}{6}} \cos \left[ \frac{1}{3} \tan^{-1} \left( \frac{3\sqrt{3}r}{2} \right) \right], \quad (13)$$

$$f_2^-(r) = \frac{2}{\sqrt{3}} \left( 1 + \frac{27}{4}r^2 \right)^{\frac{1}{6}} \sin \left[ \frac{1}{3} \tan^{-1} \left( \frac{3\sqrt{3}r}{2} \right) \right], \quad (14)$$

and when  $Q_0 = 0$ ,

$$f_1^0(r) = 2^{\frac{1}{3}} \left[ \frac{3\sqrt{3}}{2} r \right]^{-\frac{2}{3}}, \quad (15)$$

$$f_2^0(r) = \frac{2^{2/3}}{3\sqrt{3}} \left[ \frac{3\sqrt{3}}{2} r \right]^{\frac{1}{3}}. \quad (16)$$

Applying the same trick to material line evolution, we take the derivative of Eq. 2 with respect to time, giving (see also [21])

$$\frac{d^2 l_i}{dt^2} = A_{ij} A_{jk} l_k + (-A_{ik} A_{kj} - \frac{2}{3} Q \delta_{ij}) l_j = -\frac{2}{3} Q l_i. \quad (17)$$

Thus  $l_i$  satisfies the same equation as  $A_{ij}$  (see Eq. 9), and hence has the same general solution. In terms of the dimensionless variables, we write the solution as

$$l_i(\tau) = h_i f_1[r(\tau)] + g_i f_2[r(\tau)], \quad (i = 1, 2, 3) \quad (18)$$

where  $h_i$  and  $g_i$  are constants. Given initial conditions  $l_i(0)$ , and  $dl_i(0)/dt \equiv a_{ij}(0)l_j(0)$ , the coefficients can be fixed in terms of  $l_i(0)$  and  $a_{ij}(0)$ .

## 2.2. Asymptotic evolution of the material lines

The RE solution for  $A_{ij}$  diverges in finite time, but the geometry of the velocity gradient  $a_{ij}$  displays interesting universal properties asymptotically when approaching the singularity [18, 20], as is summarized in the introduction. Generalizing the method in [20], we now show that the line element  $l_i$  also exhibits certain universal geometrical properties, regardless its initial conditions.

We illustrate the method with the case where  $Q_0 = 0$ . The other two cases can be worked out in the same way. When  $Q_0 = 0$ ,  $f_1$  and  $f_2$  are denoted as  $f_1^0$  and  $f_2^0$  and given by Eqs. 15 and 16. It is also known that  $r(\tau)$  tends to positive infinity at time  $\tau = \sqrt{3}$  (see [20]). Using Eqs. 15 and 16, it is shown in [20] that

$$\lim_{r \rightarrow +\infty} a_{ij}(r) = K_{ij} r^{1/3}, \quad K_{ij} = (2^{1/3}/3) D_{ij}. \quad (19)$$

Thus the geometrical structure of  $a_{ij}$  is determined by  $K_{ij}$  when approaching the singularity. We will identify  $K_{ij}$  with the asymptotic velocity gradient, even though they differ by a scaling factor  $r^{1/3}$ . Note that  $a_{ij}(r)$  has to satisfy Eq. 6. Substituting  $a_{ij}(r) = K_{ij} r^{1/3}$  into the equation, and noting  $q = -(3\sqrt{3}r/2)^{2/3}$  in this case due to Eq. 8, one finds

$$K_{im} K_{mj} + (1/2^{1/3}) K_{ij} - 2^{1/3} \delta_{ij} = 0, \quad (20)$$

which is Eq. 78 in [20]. Due to Eq. 20,  $K_{ij}$  has rather specific structures, which has been discussed in [20] and will be used later.

We now look into the limit of the solution for  $l_i$  given by Eq. 18. It is easy to see that

$$\lim_{r \rightarrow +\infty} l_i(r) = n_i r^{1/3}, \quad n_i = (2^{1/3}/3) g_i. \quad (21)$$

Therefore  $l_i$  points to the same direction as  $n_i$  when its length tends to infinity. Now note that  $l_i$  must satisfy Eq. 2. Thus, we substitute Eqs. 21 and 19 into Eq. 2. After some algebra, we find

$$K_{ij}n_j = 2^{-1/3}n_i. \quad (22)$$

Thus, *the line element asymptotically becomes an eigenvector of the velocity gradient tensor with eigenvalue  $\lambda^l = 2^{-1/3}$* . Same limit is found for  $Q_0 > 0$  with  $n_i = 2^{2/3}g_i$ , and for  $Q_0 < 0$  with  $n_i = (3h_i/2 + g_i)2^{-1/3}$ .

A few immediate remarks can be made. First, the above result is independent of the initial orientation or length of the line element. The initial condition affects the length of the element, but not the direction. Second, Eq. 22 implies that, asymptotically, the normalized stretching rate of the material line is  $\lambda^l = 2^{-1/3}$  (c.f. Eq. 3). We will compare  $\lambda^l$  with the eigenvalues of the strain rate tensor corresponding to  $K_{ij}$  below.

To further explore the consequences of Eq. 22, we make use of the results regarding  $K_{ij}$  detailed in [20], which is derived from Eq. 20. In the eigenframe of the strain rate tensor of  $K_{ij}$ , it can be written as

$$K_{ij} = \begin{bmatrix} S_{11} & -\omega_3/2 & \omega_2/2 \\ \omega_3/2 & S_{22} & -\omega_1/2 \\ -\omega_2/2 & \omega_1/2 & S_{33} \end{bmatrix}, \quad (23)$$

where  $S_{11}$  etc are the strain rates, and  $\omega_i$  the vorticity components.  $S_{33} = -(S_{11} + S_{22})$  due to incompressibility. In order for  $K_{ij}$  to satisfy Eq. 20, there are only two possibilities, each implying different properties for  $n_i$ .

In the first one, the vorticity is zero and

$$(S_{11}, S_{22}, S_{33}) = (2^{-1/3}, 2^{-1/3}, -2^{2/3}). \quad (24)$$

Thus  $K_{ij} = \text{diag}(2^{-1/3}, 2^{-1/3}, -2^{2/3})$ . Solving Eq. 22, we find that the equation can be true only when  $n_3 = 0$ . Therefore, the material line is perpendicular to  $S_{33}$  and lies in the plane spanned by the two stretching directions, but no preferred alignment with either direction can be concluded. Moreover, the stretching rate experienced by the line element,  $\lambda^l$ , is the same as the two positive eigenvalues of the strain rate tensor.

In the second scenario, only one component of the vorticity is non-zero. Let us assume  $\omega_1 \neq 0$  and  $\omega_2 = \omega_3 = 0$ . It is then shown in [20] that  $S_{11} = 2^{-1/3}$ ,  $S_{22} > S_{11}$ , and  $S_{33} < 0$ . Thus  $S_{11}$  is the intermediate eigenvalue. Therefore, the results imply that *the stretching rate for the line element is the same as the intermediate eigenvalue of the strain rate tensor*. Besides, using these results and Eq. 22, we find that

$$n_i = (n_1, n_2, \delta n_2) = n_2(n_1/n_2, 1, \delta) \quad \text{where} \quad \delta = \frac{\omega_1}{2S_{22} + 2^{5/3}}. \quad (25)$$

The orientation of  $n_i$  hence depends on two parameters  $n_1/n_2$  and  $\delta$ , the latter measuring the relative magnitude of the vorticity. As a result, it is not straightforward to predict the behaviors. One may argue that for fixed  $n_1/n_2$ , the

alignment with the contracting eigendirection (the third coordinate direction) would increase with  $\delta$  (i.e., the relative magnitude of vorticity). The results reported in [6] appear to support the observation (see Fig. 12 therein).

To summarize, the analysis of the evolution of material lines based on the restricted Euler dynamics of the velocity gradient predicts that, asymptotically, the stretching rate tends to the intermediate eigenvalue of the strain rate tensor. This observation is supported by the DNS results in, say, [4, 6], where it has been qualitatively attributed to the effects of the vorticity and the rotation of strain axes. Our analysis suggests that these effects are captured by the restricted Euler approximation. Our analysis also predicts that, when vorticity is relatively weak, the line element tends to be perpendicular to the contracting direction of the strain rate tensor. The model does not predict a preferred alignment with the intermediate eigendirection. This observation indicates that the anisotropic part of the pressure Hessian plays a role in its origin. This is addressed in the next section with DNS data.

It is worth pointing out that the results for material lines are different from those for vorticity in several aspects, as is described above, although the asymptotic stretching rates are the same.

### 3. Analysis of the dynamics of alignment with DNS data

We now turn to the analyses of the alignment between a material element and the strain rate tensor, using a DNS data set. We will pay particular attention to the pressure Hessian term.

To consider the alignment problem, we introduce the eigenframe of the strain rate tensor  $S_{ij}$ . The alignment evolves with the strain tensor, which is governed by the following equation

$$\frac{dS_{ij}}{dt} = -S_{ik}S_{kj} - \frac{1}{4}(\omega_i\omega_j - \delta_{ij}\omega_k\omega_k) - \partial_{ij}^2 p + \nu\nabla^2 S_{ij}. \quad (26)$$

We denote the eigenvalues of the strain rate tensor as  $\lambda_1^s \geq \lambda_2^s \geq \lambda_3^s$ , and corresponding eigenvectors  $\mathbf{e}_1^s$ ,  $\mathbf{e}_2^s$ , and  $\mathbf{e}_3^s$ . The coordinate frame defined by the eigenvectors will be called the S-frame. The frame rotates as  $S_{ij}$  evolves. Let  $\boldsymbol{\Omega}^s$  be the angular velocity of the eigenframe, we have the the following relations

$$\frac{d\mathbf{e}_i^s}{dt} = \boldsymbol{\Omega}^s \times \mathbf{e}_i^s, \quad \frac{d\mathbf{e}_i^s}{dt} \cdot \mathbf{e}_j^s = \epsilon_{ijk}\Omega_k^s, \quad (27)$$

where  $\Omega_k^s$  is the  $k$ th component of  $\boldsymbol{\Omega}^s$  in the S-frame. Given the orthogonality of the eigenvectors, one has

$$\mathbf{e}_i^{sT} \mathbf{S} \mathbf{e}_j^s = 0 \quad (i \neq j), \quad (28)$$

where  $\mathbf{S}$  represents the strain rate tensor. Taking the derivative of the relation and using Eq. 27, we find

$$\frac{1}{\lambda_i^s - \lambda_j^s} \mathbf{e}_i^{sT} \frac{d\mathbf{S}}{dt} \mathbf{e}_j^s = \epsilon_{ij} \Omega_k^s, \quad (29)$$

see also[5]. Thus, using Eq. 26, we find

$$\epsilon_{ijk}\Omega_k^s = \frac{1}{\lambda_i^s - \lambda_j^s} \left[ -\frac{1}{4}\omega_i^s\omega_j^s - P_{ij}^s + V_{ij}^s \right], \quad (30)$$

where

$$P_{ij}^s \equiv \mathbf{e}_i^{sT} \mathbf{\Pi} \mathbf{e}_j^s, \quad V_{ij}^s \equiv \mathbf{e}_i^{sT} (\nu \nabla^2 \mathbf{S}) \mathbf{e}_j^s. \quad (31)$$

$P_{ij}^s$  is the  $(i, j)$  component of the pressure Hessian in the S-frame, with  $\mathbf{\Pi}$  representing the pressure Hessian tensor. The components of  $\mathbf{\Pi}$  in the fixed laboratory frame are  $\partial_{ij}^2 p$ .  $V_{ij}^s$  is the component of the diffusion term for  $\mathbf{S}$  in the S-frame.  $\omega_i^s$  is the  $i$ th component of the vorticity in the S-frame. Eq. 30 is valid only when  $i \neq j$ . Out of the 6 valid equations only three are independent, which give the expressions for the three components of the angular velocity.

Eq. 30 shows that the rotation of the S-frame is induced by vorticity, the pressure Hessian and viscous diffusion. Because  $i \neq j$ ,  $P_{ij}^s$  only contains contributions from the anisotropic part.

The evolution of a line element can be described by the deformation gradient  $B_{ij}$ , which evolves according to Eq. 4. We will solve Eq. 4 numerically to find  $B_{ij}$ . With  $B_{ij}$  given, we then find the CG tensor and its eigenvectors and eigenvalues. As is known from [4], the alignment statistics of the eigenvector corresponding to the largest eigenvalue of  $C_{ij}$  show same trends as those of a line element. We will thus only investigate the former.

We use  $\lambda_1^c \geq \lambda_2^c \geq \lambda_3^c$  to denote the eigenvalues of  $\mathbf{C}$ ,  $\mathbf{e}_1^c$ ,  $\mathbf{e}_2^c$  and  $\mathbf{e}_3^c$  the corresponding eigenvectors, and  $\mathbf{\Omega}^c$  angular velocity of the eigenframe of  $\mathbf{C}$ . The eigenframe will be called the C-frame, to distinguish it from the S-frame. The eigenvalues are all positive since the CG tensor is positive definite. Note that a relation similar to Eq. 28 exists for  $\mathbf{C}$  and its eigenvectors. Using that, we find the expressions for the components of  $\mathbf{\Omega}^c$  in the C-frame, which can be written as

$$\epsilon_{ijk}\Omega_k^c = \frac{\lambda_i^c + \lambda_j^c}{\lambda_i^c - \lambda_j^c} S_{ij}^c + \epsilon_{ijk} \frac{\omega_k^c}{2} \quad (32)$$

In the equation  $S_{ij}^c$  and  $\omega_k^c$  are the components of the strain rate tensor and vorticity in the C-frame, respectively. Eq. 32 is also only valid for  $i \neq j$ .

Eq. 32 shows that, apart from the vorticity, straining also contributes to the rotation of a material element by changing its shape. Note that  $\omega_k^c \neq \omega_k^s$  even for the same vorticity vector, because they represent the  $k$ th component in different coordinate frames.

The quantities that we are interested in are the direction cosines  $\alpha_i = |\mathbf{e}_1^c \cdot \mathbf{e}_i^s|$  for  $i = 1, 2, 3$ . A close alignment between  $\mathbf{e}_1^c$  with the intermediate eigenvector of  $S_{ij}$  implies that there is a strong peak at  $\alpha_2 = 1$  in the probability density function (PDF) of  $\alpha_2$ . We will consider the PDF of  $\alpha_i$ , denoted as  $P(\alpha_i)$ . We will derive the equation governing its evolution and elucidate the dynamics leading to the preferential alignment.

Using Eq. 27 and a similar equation for  $\mathbf{e}_1^c$ , it is not difficult to find

$$\frac{d\alpha_i}{dt} = \text{sign}(\mathbf{e}_1^c \cdot \mathbf{e}_i^s) (\mathbf{\Omega}^s - \mathbf{\Omega}^c) \cdot (\mathbf{e}_i^s \times \mathbf{e}_1^c). \quad (33)$$

The equation shows that the evolution of  $\alpha_i$  is determined by the difference between the angular velocities projected on a direction perpendicular to both eigendirections. According to Eqs. 30 and 32, there are five contributions to the right hand side of Eq. 33. We use  $R_o^s$ ,  $R_p^s$ , and  $R_v^s$  to denote the contributions from the three terms on the right hand side of Eq. 30, and use  $R_o^c$  and  $R_s^c$  to denote the vorticity and strain rate contributions, respectively, from Eq. 32. We have from Eq. 32

$$R_o^c = -\frac{1}{2}\boldsymbol{\omega} \cdot (\mathbf{e}_i^s \times \mathbf{e}_1^c)\text{sign}(\mathbf{e}_1^c \cdot \mathbf{e}_i^s). \quad (34)$$

Other quantities would take a similar form after suitable notations are introduced. For example, define vector  $\mathbf{h}$  by

$$h_k = -\frac{1}{2}\epsilon^{kij}\frac{P_{ij}^s}{\lambda_i^s - \lambda_j^s}. \quad (35)$$

Then

$$R_p^s = \mathbf{h} \cdot (\mathbf{e}_i^s \times \mathbf{e}_1^c)\text{sign}(\mathbf{e}_1^c \cdot \mathbf{e}_i^s). \quad (36)$$

We will use  $R$  to denote the sum of all the contributions, i.e.,  $R = \text{sign}(\mathbf{e}_1^c \cdot \mathbf{e}_i^s)(\boldsymbol{\Omega}^s - \boldsymbol{\Omega}^c) \cdot (\mathbf{e}_i^s \times \mathbf{e}_1^c)$ . These quantities are termed ‘‘effective rotation’’ for convenience.

The equation for  $P(\alpha_i)$  can now be derived from Eq. 33 (see, e.g. [27]), which reads

$$\frac{\partial P}{\partial t} = -\frac{\partial}{\partial \alpha_i} (\langle R|\alpha_i \rangle P), \quad (37)$$

where  $\langle R|\alpha_i \rangle$  is the average of  $R$  conditioned on given value  $\alpha_i$ . Physically,  $\langle R|\alpha_i \rangle$  is the conditional rate of change of  $\alpha_i$  (cf. Eq. 33). Its product with  $P(\alpha_i)$  gives the probability flux across  $\alpha_i$ . Eq. 37 shows that, where the gradient of  $\langle R|\alpha_i \rangle P(\alpha_i)$  is negative, the probability accumulates hence PDF increases with time. Thus, the evolution of  $P(\alpha_i)$  can be learned from the distributions of the probability fluxes.

We document below the conditional statistics in a DNS data set, and investigate the behaviors of the five different contributions to  $R$ .

### 3.1. Numerical simulations

We solve the forced Navier-Stokes equations using a pseudo-spectral method in a  $[0, 2\pi]^3$  periodic box. Time-marching is conducted with the AB2 method. The Courant number defined with the maximum speed in the velocity field is set at  $\beta = 0.3$ . The resolution of the data is  $128^3$ , with the viscosity  $\nu = 0.006$ . The forcing term injects energy into the flow field in such a way that the mean dissipation is maintained at 0.1. For these parameters, the Kolmogorov time scale in the resulted flow fields is  $\tau_\eta \approx 0.25$ . The Reynolds number based on the Taylor length scale is about 60. The Kolmogorov length scale is  $\eta \approx 0.04$ , such that  $k_{\max}\eta \approx 1.6$  ( $k_{\max} \approx 43$  due to dealiasing by the two-third rule).

Velocity data are saved at a constant time interval after the statistics have reached steady state. The time interval is set as  $\Delta t_w = 0.01225$ , corresponding to Courant number  $\beta \approx 0.5$ . The corresponding pressure fields are also computed and stored.

Particle tracking is performed using the saved snapshots of the velocity fields (thus the time step size is  $\Delta t_w$ ). The deformation gradient is solved along the particle trajectories. AB2 is used to solve for the trajectories, and a fourth order predictor-corrector method proposed in [4] is used to integrate the equation for the deformation gradient. We use a sixth order Lagrange interpolation scheme to find the parameters on the fluid particles. To solve the equation for the deformation gradient, we need the velocity gradient at the spatial location of the fluid particles. They are found by interpolation from grid-point values after the latter is found with Fourier transforms.

$128^3$  particles are released in the flow field at 22 well-separated times. They are tracked over a time span approximately equal  $8\tau_\eta$ . Thus there are  $22 \times 128^3$  trajectories in total, and the statistics are averaged over all the trajectories.

### 3.2. Numerical data and analysis

Due to the dispersive nature of turbulence, the evolution of a material element is a non-stationary process. However geometrical statistics tend to reach a stationary distribution within few Kolmogorov time scales, after an initial transience [4]. We will present results at  $t = 1.22, 3.68, 7.35\tau_\eta$ . The statistics at the last time essentially represent the behaviors at the stationary stage, although small residual evolution can be seen (A recent study in a slightly different context [28] shows that some small changes can be seen up to time  $t \sim 12\tau_\eta$ ).

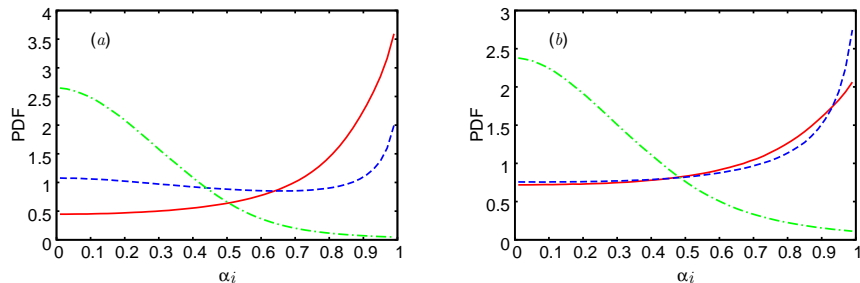


Figure 1: The PDFs of  $\alpha_i = |\mathbf{e}_1^c \cdot \mathbf{e}_i^s|$  at (a)  $t = 3.68\tau_\eta$  and (b)  $t = 7.35\tau_\eta$ . Solid line:  $i = 1$  (the strongest stretching direction of  $S_{ij}$ ); dashed line:  $i = 2$  (intermediate direction); dash-dotted line:  $i = 3$  (contracting direction).

We present in Fig. 1 the PDFs for the alignment between  $\mathbf{e}_1^c$  and the S-frame, i.e.,  $P(\alpha_i)$ , calculated from our data. At very short time  $\delta t$ ,  $C_{ij}(\delta t) \approx \delta_{ij} + 2\delta t S_{ij}$ . Thus  $C_{ij}$  has perfect alignment with  $S_{ij}$ , where  $\mathbf{e}_1^c$  is in the same direction as  $\mathbf{e}_1^s$  and perpendicular to  $\mathbf{e}_2^s$  and  $\mathbf{e}_3^s$ . The alignment relaxes over time. The alignment between  $\mathbf{e}_1^c$  and  $\mathbf{e}_2^s$  increases while that between  $\mathbf{e}_1^c$  and  $\mathbf{e}_1^s$  weakens, leading to the results in Fig. 1(a). Fig. 1(b) shows that the  $\mathbf{e}_1^c - \mathbf{e}_2^s$

alignment finally dominates, while  $\mathbf{e}_1^c$  and  $\mathbf{e}_1^s$  remains a rather strong tendency to align with each other. On the other hand,  $\mathbf{e}_1^c$  always tends to be perpendicular to  $\mathbf{e}_3^s$  with large probabilities. These observations confirm what has been found in previous investigations (see, e.g., [6]).

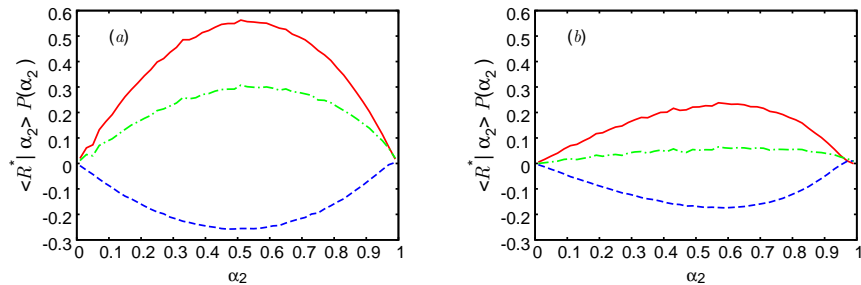


Figure 2: The probability flux  $\langle R^* | \alpha_2 \rangle P(\alpha_2)$  for  $\mathbf{e}_1^c - \mathbf{e}_2^s$  alignment at (a)  $t = 3.68\tau_\eta$  and (b)  $t = 7.35\tau_\eta$ . Solid line:  $R^* = R_o^s + R_p^s + R_v^s$  (total contribution from the rotation of the S-frame); dashed line:  $R^* = R_o^c + R_s^c$  (total contribution from the rotation of the C-frame); dash-dotted line:  $R^* = R$  (total).

Our goal is to understand the evolution shown in Fig. 1. We thus look into the conditional statistics that control the preferential  $\mathbf{e}_1^c - \mathbf{e}_2^s$  alignment. We plot in Fig. 2 the conditional averaged effective rotations for  $\alpha_2$  weighted by the PDF  $P(\alpha_2)$ , ie., the probability fluxes. The total value and those from the rotation of the S-frame and the C-frame are plotted separately. According to Eq. 37, the PDF for  $\alpha_2$  increases where the gradient of the weighted conditional average of  $R$  is negative, and vice versa. The dash-dot curve in Fig. 2(a) has a negative gradient for  $\alpha_2 > 0.6$ , which shows that the probability for preferential alignment  $\alpha_2 > 0.6$  increases. The same trend remains at  $t = 7.35\tau_\eta$  (Fig. 2(b)), but with a rather weaker rate, indicative of reaching stationary distribution. These behaviors are consistent with Fig. 1. The results for the separate contributions exhibit interesting difference. The contribution from the rotation of the S-frame shows the same trend as the total contribution. Namely, it always tends to strengthen the  $\mathbf{e}_1^c - \mathbf{e}_2^s$  alignment. On the other hand, the rotation of the C-frame always tends to weaken the alignment. The behavior is observed at both times.

The contributions from the rotation of the two frames are presented in Fig. 3. Plotted in Fig. 3(a) are the three contributions to the rotation of the S-frame. The figure shows that both vorticity (solid line) and the non-local pressure Hessian work to strengthen the  $\mathbf{e}_1^c - \mathbf{e}_2^s$  alignment, since the two curves mostly have negative gradients for large  $\alpha_2$ . The viscous term makes a small, opposite contribution. The two contributions to the rotation of the C-frame is given in Fig. 3(b). Here vorticity tends to increase the alignment as well, as is shown by the solid line. The effect is weaker compared with the vorticity contribution in Fig. 3(a), since the slope of the curve is flatter. This contribution, however, is dominated by the counteracting contribution from straining, shown by the dashed line. In other words, the straining of the material element tends to strongly tilt

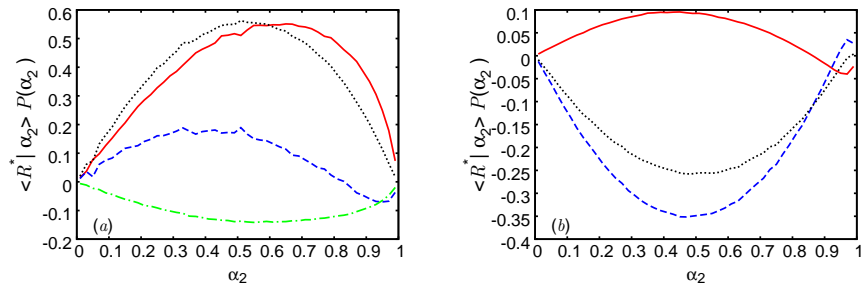


Figure 3: The probability fluxes  $\langle R^* | \alpha_2 \rangle P(\alpha_2)$  for  $\mathbf{e}_1^c - \mathbf{e}_2^s$  alignment at  $t = 3.68\tau_\eta$ . (a) Solid line:  $R^* = R_o^s$ ; dashed:  $R^* = R_p^s$ ; dash-dotted:  $R^* = R_v^s$ ; dotted: the sum of previous three. (b) Solid line:  $R^* = R_o^c$ ; dashed:  $R^* = R_s^c$ ; dotted: the sum of previous two.

$\mathbf{e}_1^c$  away from  $\mathbf{e}_2^s$ . Thus, both Fig. 3(a) and (b) show consistently that, whilst vorticity tends to enhance the alignment, straining does the opposite.

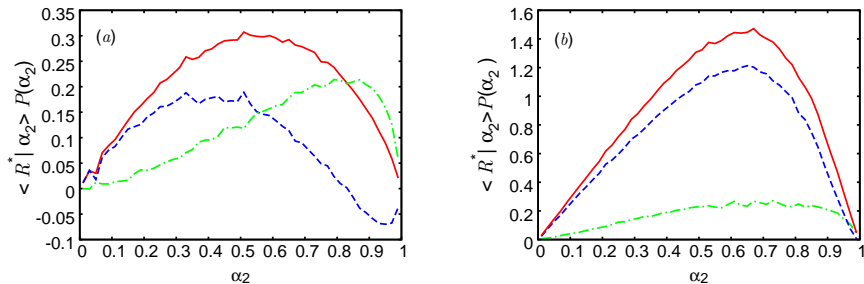


Figure 4: The probability fluxes  $\langle R^* | \alpha_2 \rangle P(\alpha_2)$  for  $\mathbf{e}_1^c - \mathbf{e}_2^s$  alignment at (a)  $t = 3.68\tau_\eta$  (b)  $t = 1.22\tau_\eta$ . Solid line:  $R^* = R$  (total); dashed:  $R^* = R_p^s$ ; dash-dotted:  $R^* = R - R_p^s$ .

To assess the relative importance of the pressure Hessian term, we compare it with the combination of all the other four contributions, which mainly come from straining-and-vorticity-induced rotation (of the two frames) and will be referred to as local effects. Fig. 4(a) shows, respectively, the conditional rate of change of  $\alpha_2$  generated from the pressure Hessian (dashed line) and that from local effects (dash-dotted line), at  $t = 3.68\tau_\eta$ . The total value is plotted with solid line as a reference. We first observe that the magnitudes for the two distributions are comparable, thus the non-local pressure Hessian indeed has significant effects. The curve for local effects has a steep negative slope near  $\alpha_2 = 1$ , implying that they have a strong effect in generating the  $\mathbf{e}_1^c - \mathbf{e}_2^s$  alignment. Meanwhile, the distribution for pressure Hessian has a positive slope at  $\alpha_2 = 1$ . Thus, it does not prefer the perfect alignment between  $\mathbf{e}_1^c$  and  $\mathbf{e}_2^s$ , although overall it tends to improve their alignment, since the curve mostly has negative slope when  $\alpha_2 > 0.5$ .

On the other hand, for  $\alpha_2$  around 0, the pressure Hessian contribution has a steeper positive slope compared with that of the local effects. This means that

the non-local pressure Hessian is more effective at bringing  $\mathbf{e}_1^c$  and  $\mathbf{e}_2^s$  closer when they are nearly perpendicular. This interpretation is corroborated by Fig. 4(b). In (b) the comparison is made at an earlier time  $t = 1.22\tau_\eta$ . At this stage  $\mathbf{e}_1^c$  dominantly aligns with  $\mathbf{e}_1^s$  and tends to be perpendicular to  $\mathbf{e}_2^s$ . The figure shows that the contribution from pressure Hessian is much stronger, as is expected from the above interpretation.

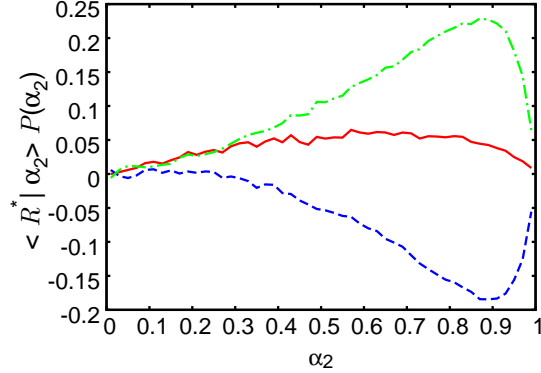


Figure 5: Same as Fig. 4(a) but for  $t = 7.35\tau_\eta$ .

Fig. 5 plots same comparison as Fig. 4(a) at  $t = 7.35\tau_\eta$ . The total contribution now is nearly zero as the PDF is reaching the stationary distribution. Compared with Fig. 4(a), the local effects remain nearly the same except the magnitude has decreased slightly. On the other hand, the non-local pressure Hessian has evolved to counteract the local effects. Namely, the pressure Hessian now acts to destroy the  $\mathbf{e}_1^c - \mathbf{e}_2^s$  alignment, with a sharp positive slope at  $\alpha_2 = 1$ .

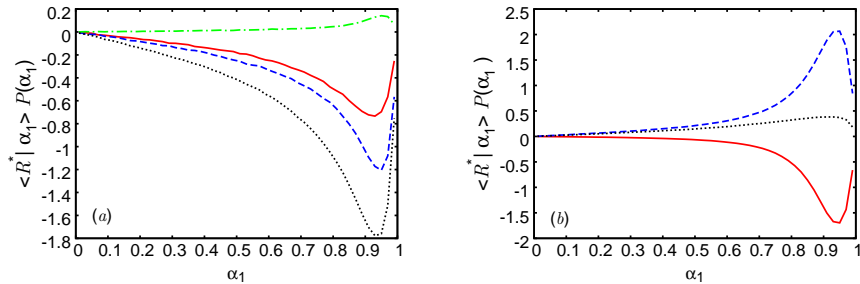


Figure 6: The probability fluxes  $\langle R^* | \alpha_1 \rangle P(\alpha_1)$  for  $\mathbf{e}_1^c - \mathbf{e}_1^s$  alignment at  $t = 1.22\tau_\eta$ . (a) Contributions from the rotation of the S-frame. Solid line:  $R^* = R_o^s$ ; dashed line:  $R^* = R_p^s$ ; dash-dotted line:  $R^* = R_v^s$ ; dotted line: total contribution. (b) Contributions from the rotation of the C-frame. Solid line:  $R^* = R_o^c$ ; dashed line:  $R^* = R_s^c$ ; dotted line: total contribution.

It is instructive to also consider the results for the alignment between  $\mathbf{e}_1^c$  and  $\mathbf{e}_1^s$ . Fig. 6 shows the results for the probability fluxes at a short time

$t = 1.22\tau_\eta$ . Note that initially the  $\mathbf{e}_1^c - \mathbf{e}_1^s$  alignment is perfect, and  $P(\alpha_1)$  has a strong peak at  $\alpha_1 = 1$ . The total contributions from the rotation of the S-frame and C-frame are given by the dotted line in Fig. 6(a) and (b), respectively. Overall the rotation of the S-frame will reduce the peak strongly, as shown by the steep negative slope near  $\alpha_1 = 1$ . On the other hand, the rotation of the C-frame tends to maintain the peak. For the rotation of the S-frame, Fig. 6(a) shows the contributions mainly come from vorticity and pressure Hessian, the latter dominating the former. Viscous diffusion tends to maintain the alignment, but the effect is weak. For the rotation of the C-frame, Fig. 6(b) shows that vorticity tends to reduce the alignment. However, the straining-induced rotation produces an even stronger effect to reinforce the alignment.

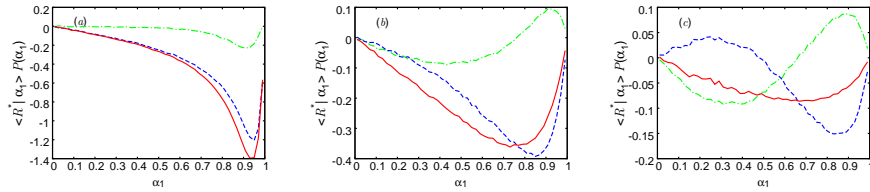


Figure 7: The probability fluxes  $\langle R^* | \alpha_1 \rangle P(\alpha_1)$  for  $\mathbf{e}_1^c - \mathbf{e}_1^s$  alignment at (a)  $t = 1.22\tau_\eta$ , (b)  $t = 3.68\tau_\eta$  and (c)  $t = 7.35\tau_\eta$ . Dashed line:  $R^* = R_p^s$ ; dash-dotted line:  $R^* = R - R_p^s$ ; solid line: total contribution.

The qualitative features shown in Fig. 6 are maintained at later times. We now show the comparison between pressure Hessian and the total of other local effects in Fig. 7(a), (b) and (c) for  $t = 1.22, 3.68$  and  $7.35\tau_\eta$ , respectively. It is clear from the results that the pressure Hessian is the main cause for the reduction of the  $\mathbf{e}_1^c - \mathbf{e}_1^s$  alignment (with steep positive slope near  $\alpha_1 = 1$ ). The effect persists throughout the evolution. On the other hand, the local effects initially also help reduce the alignment, but then turn to to enhance it at later time. The two contributions almost balance each other in the end, as is shown in Fig. 7(c).

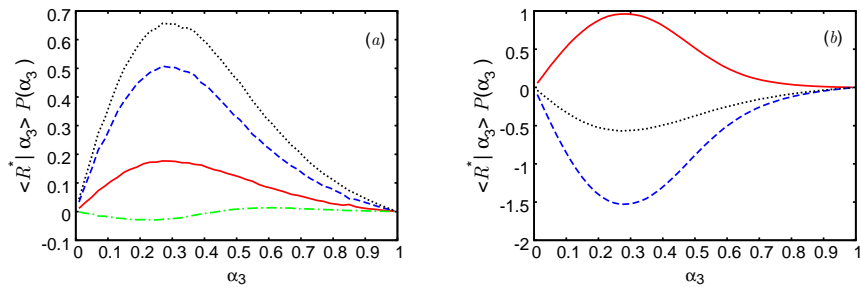


Figure 8: The probability fluxes  $\langle R^* | \alpha_3 \rangle P(\alpha_3)$  for  $\mathbf{e}_1^c - \mathbf{e}_3^s$  alignment at  $t = 3.68\tau_\eta$ . (a) Contributions from the rotation of the S-frame. Solid line:  $R^* = R_o^s$ ; dashed line:  $R^* = R_p^s$ ; dash-dotted line:  $R^* = R_v^s$ ; dotted line: total contribution. (b) Contributions from the rotation of the C-frame. Solid line:  $R^* = R_o^c$ ; dashed line:  $R^* = R_s^c$ ; dotted line: total contribution.

Finally, we briefly discuss the  $\mathbf{e}_1^c - \mathbf{e}_3^s$  alignment, shown in Fig. 8. As is shown in Fig. 1,  $\mathbf{e}_1^c$  initially is perfectly perpendicular to  $\mathbf{e}_3^s$ , and remains preferentially so later on. Therefore we focus on the behaviors near  $\alpha_3 = 0$  when examining Fig. 8. First of all, we observe that the effect of vorticity (shown by solid lines in both (a) and (b)) is always reducing the probability for the perpendicular configuration, since the curves have positive slopes at  $\alpha_3 = 0$ . This is in line with the prediction from the restricted Euler approximation (see Eq. 25 and the discussion that follows) and previous research [6]. Pressure Hessian, shown by the dashed line in Fig. 8(a), also tends to reduce the probability for  $\alpha_3 = 0$ , and the effect is rather strong. On the other hand, the dashed line in Fig. 8(b) shows that the straining-induced rotation of the C-frame will in effect strengthen the perpendicular configuration.

#### 4. Conclusions

We have investigated the properties of geometrical alignment in the evolution of material elements in isotropic turbulence. We first present an analysis based on the restricted Euler approximation, and look into the asymptotic stretching rate and alignment trends for material line elements. The result predicts that the stretching rate would be given by the intermediate eigenvalue of the strain rate tensor. The prediction is consistent with well-known observations in numerical simulations of isotropic turbulence. The alignment properties between a material element and the strain rate tensor is then analyzed using DNS data. The individual contributions to the rotation of the eigenframes of the strain rate tensor as well as the Cauchy-Green tensor are documented. Emphasis is given to the effects of the pressure Hessian.

The results show that the pressure Hessian is the main cause for the misalignment between the longest axis of the Cauchy-Green tensor and the strongest stretching eigendirection of the strain rate (the 1-1 alignment). This effect persists throughout the evolution. In the meantime, it facilitates the alignment between the longest axis of the Cauchy-Green tensor and the intermediate eigendirection of the strain rate (the 1-2 alignment) during initial evolution. However, its role changes to resist the 1-2 alignment later.

Vorticity-induced rotation of both eigenframes prefers 1-2 alignment and suppresses 1-1 alignment, whereas straining-induced rotation does exactly the opposite. The two effects partially cancel each other, and the net effect is that both alignments are enhanced.

The effects of the pressure Hessian can not be trivially reduced to its effects on the rotation of the eigenframe of the strain rate tensor, since they strongly depend on the relative orientation of the two eigenframes and evolve with deformation. Our results shed some light on the interesting effects on the coupling between the three entities. More questions remain to be answered, such as the geometrical alignment between the pressure Hessian and the material elements, which may help understand the interesting roles of the former. This, and related questions, will be the subject of further studies.

- [1] G. K. Batchelor, The effects of homogeneous turbulence on material lines and surfaces, *Proceedings of the Royal Society of London. Series A, Mathematical and Physical Sciences* 213 (1952) 349–366.
- [2] W. J. Cocke, Turbulent hydrodynamic line stretching: consequences of isotropy, *Phys. Fluids* 12 (1969) 2488–2492.
- [3] S. A. Orszag, Comments on “Turbulent hydrodynamic line stretching: consequences of isotropy”, *Phys. Fluids* 13 (1970) 2203–2204.
- [4] S. S. Girimaji, S. B. Pope, Material element deformation in isotropic turbulence, *J. Fluid Mech.* 220 (1990) 427–458.
- [5] E. Dresselhaus, M. Tabor, The kinematics of stretching and alignment of material elements in general flow fields, *J. Fluid Mech.* 236 (1991) 415–444.
- [6] M. J. Huang, Correlations of vorticity and material line elements with strain in decaying turbulence, *Phys. Fluids* 8 (1996) 2203–2214.
- [7] J. Duplat, E. Villermaux, Persistency of material element deformation in isotropic flows and growth rate of lines and surfaces, *Eur. Phys. J. B* 18 (2000) 353–361.
- [8] S. Kida, S. Goto, Line statistics: Stretching rate of passive lines in turbulence, *Phys. Fluids* 14 (2002) 352–361.
- [9] K. Ohkitani, Numerical study of comparison of vorticity and passive vectors in turbulence and inviscid flows, *Phys. Rev. E* 65 (2002) 046304.
- [10] M. Guala, B. Lüthi, A. Liberzon, A. Tsinober, W. Kinzelbach, On the evolution of material lines and vorticity in homogeneous turbulence, *J. Fluid Mech.* 533 (2005) 339–359.
- [11] S. Goto, S. Kida, Reynolds-number dependence of line and surface stretching in turbulence: folding effects, *J. Fluid. Mech.* 586 (2007) 59–81.
- [12] M. Chertkov, A. Pumir, B. I. Shraiman, Lagrangian tetrad dynamics and the phenomenology of turbulence, *Phys. Fluids* 11 (1999) 2394–2410.
- [13] E. Jeong, S. S. Girimaji, Velocity-Gradient Dynamics in Turbulence: Effect of Viscosity and Forcing, *Theoret. Comput. Fluid Dyn.* 16 (2003) 421–432.
- [14] Y. Li, C. Meneveau, Origin of non-Gaussian statistics in hydrodynamic turbulence, *Phys. Rev. Lett.* 95 (2005) 164502.
- [15] L. Chevillard, C. Meneveau, Lagrangian dynamics and statistical geometric structure of turbulence, *Phys. Rev. Lett.* 97 (2006) 174501.
- [16] Y. Li, L. Chevillard, G. Eyink, C. Meneveau, Matrix exponential-based closures for the turbulent subgrid-scale stress tensor, *Phys. Rev. E* 79 (2009) 016305.

- [17] A. Tsinober, B. Galanti, Exploratory numerical experiments on the differences between genuine and “passive” turbulence, *Phys. Fluids* 15 (2003) 3514.
- [18] P. Vieillefosse, Local interaction between vorticity and shear in a perfect incompressible fluid, *J. Phys.* 43 (1982) 837–842.
- [19] P. Vieillefosse, Internal motion of a small element of fluid in an inviscid flow, *Physica A* 125 (1984) 150–162.
- [20] B. J. Cantwell, Exact solution of a restricted Euler equation for the velocity gradient tensor, *Phys. Fluids A* 4 (1992) 782–793.
- [21] Y. Li, C. Meneveau, Material deformation in a restricted Euler model for turbulent flows: analytic solution and numerical tests, *Phys. Fluids* 19 (2007) 015104.
- [22] L. Chevillard, C. Meneveau, L. Biferale, F. Toschi, Modeling the pressure Hessian and viscous Laplacian in Turbulence: comparisons with DNS and implications on velocity gradient dynamics, *Phys. Fluids* 20 (2008) 101504.
- [23] K. Ohkitani, Eigenvalue problems in three-dimensional Euler flows, *Phys. Fluids A* 5 (1993) 2570–2572.
- [24] K. Ohkitani, S. Kishiba, Nonlocal nature of vortex stretching in an inviscid fluid, *Phys. Fluids* 7 (1995) 411–421.
- [25] D. Chae, On the finite-time singularities of the 3D incompressible Euler equations, *Comm. Pure Appl. Math.* 60 (2007) 0597–0617.
- [26] H. Liu, E. Tadmor, Spectral dynamics of the velocity gradient field in restricted flows, *Commun. Math. Phys.* 228 (2002) 435–466.
- [27] S. B. Pope, *Turbulent flows*, Cambridge University Press, Cambridge, 2000.
- [28] A. Pumir and M. Wilkinson, Orientation statistics of small particles in turbulence, *New J. Phys.* 13 (2011) 093030.